ELSEVIER

Contents lists available at ScienceDirect

### **Applied Energy**

journal homepage: www.elsevier.com/locate/apenergy





# Enhancing sustainable urban environments in China: Daytime radiative cooling for building energy efficiency and heat island mitigation<sup>★</sup>

Ze Li, Jianheng Chen, Chuyao Wang, Wenqi Wang, Yang Fu, Xu Chen, Rui Zhang, Aiqiang Pan, Tsz Chung Ho, Kaixin Lin, Lin Liang, Chi Yan Tso  $^*$ 

School of Energy and Environment, City University of Hong Kong, Hong Kong, China

#### HIGHLIGHTS

- A new urban canopy model was developed to assess radiative cooling's impact on building energy efficiency.
- Extensive large-scale field experiments were conducted to validate the numerical model.
- Comprehensive simulations of urban canyons in 338 Chinese cities were conducted to evaluate potential energy savings.
- Applying radiative cooling in southern China achieved year-round building energy savings.

#### ARTICLE INFO

# Keywords: Cumulative energy demand Urban Heat Island mitigation Urban canopy model Urban sustainable development Passive radiative cooling

#### ABSTRACT

Rapid urbanization in China has led to a significant increase in building energy consumption, highlighting the need for effective energy-saving strategies to enhance urban sustainability. Daytime radiative cooling (RC) offers a passive cooling solution that can reduce energy consumption without electricity usage. However, practical guidance on the applicability of RC coatings across diverse urban environments and climatic conditions remains limited. In this study, a RC model was integrated into the Urban Canopy Model (UCM) and validated through extensive large-scale field experiments. By simulating urban canyons in 338 cities across China, this work evaluated the potential of RC coatings applied to urban skins (walls and pavements) to enhance building energy efficiency. The analysis reveals that implementing RC coatings can significantly lower surface temperatures by up to 35 °C in Hong Kong and up to 40 °C in certain northwestern cities. This substantial temperature reduction leads to decreased building cooling loads, offering notable energy savings across different climatic zones. Based on these findings, strategic implementations of RC pavements and walls are proposed, particularly in densely populated high-rise areas within the temperate and hot-summer/warm-winter regions of China's climate zones. This research provides actionable strategies for reducing energy consumption in the built environment.

#### 1. Introduction

Over half of the global population now resides in urban areas, a demographic shift that has significantly accelerated urbanization [1]. This demographic shift leads to the replacement of natural surfaces, such as vegetation and soil, with engineered materials, significantly altering the radiative properties of urban landscapes and enhancing solar radiation absorption [2–4]. Additionally, changes in urban architecture disrupt atmospheric convective heat transfer, while human activities increase heat generation, together leading to a significant rise in surface

temperatures. This phenomenon, known as the urban heat island (UHI) effect, is characterized by significantly higher air and surface temperatures in urban areas compared to rural regions [5–7]. The UHI effect increases electricity and water consumption in buildings [8,9], exacerbates heat stress [10,11], heightens the risk of extreme heat events [12,13], and poses significant health risks [14,15]. Consequently, the implementation of effective strategies to mitigate the UHI effect is of critical importance.

To mitigate the effects of the UHI, a variety of systems and technologies have been employed. These strategies include the

 $<sup>^{\</sup>star}$  This article is part of a Special issue entitled: 'MITAB2024 (R.R)' published in Applied Energy.

<sup>\*</sup> Corresponding author at: School of Energy and Environment, City University of Hong Kong, 83 Tat Chee Ave, Kowloon Tong, Kowloon, Hong Kong, China. E-mail address: chiytso@cityu.edu.hk (C.Y. Tso).

incorporation of additional greenery [16], the introduction of water bodies [17], and the application of innovative materials in buildings and urban spaces [18]. Among these innovative materials, recent advancements in reflective technologies for roofs and pavements have notably increased urban albedo, effectively lowering peak ambient temperatures [19]. For instance, a cool pavement program in Arizona has demonstrated the potential of high-reflectance (HR) materials to mitigate UHI [20]. Experiments have also demonstrated that reflective pavements can achieve a cooling effect of 4-6 °C. However, increasing surface solar reflectance to lower surface temperatures exposes pedestrians to more solar radiation, raising their radiant heat load. To address this issue, retro-reflective (RR) surfaces, which ideally reflect incoming sunlight back to its source or upwards under less optimal conditions, have significant potential to overcome the limitations of HR surfaces and offer additional cooling benefits [21]. The application of RR walls and pavements has been shown to reduce urban canyon surface temperatures by 20 °C and canyon air temperatures by 2.6 °C [22], significantly improving pedestrian thermal comfort, with reductions of 0.55 °C in skin temperature and 153 W·m<sup>-2</sup> in net radiation gain. Furthermore, phosphorescent (PP) coatings have been explored for their potential to mitigate surface overheating in urban areas [23], and these optimized coatings can reduce surface temperatures by up to 2.6 °C. To enhance material adaptability across all seasons, adaptive materials capable of adjusting their thermo-optical properties in response to environmental conditions have attracted considerable interest. Through global analysis, thermochromic materials on a traditional roof reduced annual cooling loads by 6.59 %, compared to 7.84 % for cool roofs [24]. However, during the colder months, the heating load on the cool roof increased by 5.87 % due to reduced passive solar heating, whereas the heat load on the thermochromic surfaces rose by only 0.07 %.

In addition to the above cooling solutions, RC has garnered considerable attention in recent years [25-30]. RC's spectral selectivity, marked by high solar reflectivity and high emissivity within the atmospheric window, makes it more effective than traditional reflective materials, significantly reducing surface temperatures and enhancing building cooling. Current studies have primarily utilized data from weather stations to evaluate the radiative cooling potential in different regions, aiming to further guide its application. In Europe, analysis of data from 1791 meteorological stations indicated that the average nocturnal cooling power is 47.30 W·m<sup>-2</sup> [31]. Similarly, in the United States, data from 1681 weather stations revealed that the annual average cooling power is approximately 50.5 W·m<sup>-2</sup>. In the southwestern U.S., the average annual cooling power can reach 70  $\mathrm{W} \cdot \mathrm{m}^{-2}$ under dry and clear sky conditions [32]. In China, based on analysis of typical annual meteorological data, the radiative cooling potential varies from 11.4  $\text{W}\cdot\text{m}^{-2}$  in the humid southeast to 63.5  $\text{W}\cdot\text{m}^{-2}$  in the arid northwest [33]. Further investigations estimated an annual maximum cooling power up to 71.9  $W \cdot m^{-2}$  in northwestern regions [34]. These findings highlight significant spatial variability in RC potential due to climatic differences, emphasizing the importance of tailoring RC applications to specific regional conditions. However, the high initial and incremental costs associated with RC coatings make their widespread application prohibitive [35]. For instance, the initial cost of RC roofing is significantly higher, with incremental costs ranging from 34.6 USD to 64.7 USD per square meter for a five-year payback period [36,37]. Consequently, modifying all urban surfaces with RC coatings is not feasible for most cities, shifting the focus to maximizing benefits through partial applications. Developing optimal strategies to achieve the greatest impact with limited resources is therefore critical. Some studies have suggested that RC coatings are particularly suitable for lightweight buildings [38] and are more economically feasible for attaining energy savings in warmer regions [39]. Despite these insights, this issue remains underexplored in the literature, leaving cities and communities without clear strategies for effective implementation.

This study performs a comprehensive assessment of the effectiveness of deploying RC coatings in urban environments to mitigate the UHI

effect. Unlike previous research that predominantly focused on rooftops and was limited in geographical scope, this investigation extends the application of RC coatings to walls and streets, incorporating the diverse climates of various Chinese cities. The coupled UCM [40] is utilized to accurately simulate local microclimates and evaluate the performance of RC coatings under different urban configurations. Based on these findings, this study proposes a strategic approach to optimize the benefits of RC coatings across diverse urban landscapes.

#### 2. Numerical model and input parameters

#### 2.1. Numerical model

The UCM [40] has been widely used to simulate surface energy transport within typical urban street canyons. As a single-layer model, it simplifies urban geometry while incorporating key processes such as building shadowing, reflection of solar radiation and infrared radiation, wind profile dynamics, and heat conduction mechanisms for roofs. walls, and ground surfaces. RC simulation requires detailed consideration of both longwave and shortwave radiation effects that naturally align with the UCM framework. To leverage this compatibility, the radiative terms in the UCM were coupled with the RC model to accurately simulate the performance of RC coatings applied to walls and ground surfaces. By explicitly accounting for shadow effects, wall-towall and wall-to-ground thermal radiation exchange, and the impact of multiple reflections of solar radiation, the integrated model captures key thermal interactions between surfaces and the urban microclimate. This approach provides a more comprehensive and long-term assessment of the practical performance of RC coatings. The specific UCM schematic is shown in Fig. 1.

#### 2.1.1. Urban canopy model

The development of the UCM is primarily based on the Princeton Urban Canopy Model [40]. The specific thermal balance equations are provided in Eq. (1).

$$R_{\rm n} + AH = Q_{\rm H} + Q_{\rm LE} + Q_{\rm G}, \tag{1}$$

where  $R_n$  is the net radiation. AH is the heat flux generated by human activities.  $Q_H$ ,  $Q_{LE}$ ,  $Q_G$  correspond to the heat transfer by convection, evaporation, and conduction, respectively.

The solar azimuth angle  $\theta_{az}$ , solar zenith angle  $\theta_z$ , solar hour angle  $\omega_t$ , and solar declination  $\delta$  can be calculated via Eqs. (2)–(5),

$$\cos\theta_{\rm az} = \frac{\cos\theta_{\rm z}\sin\varphi - \sin\delta}{\cos\theta_{\rm z}\cos\varphi},\tag{2}$$

$$\cos\theta_{z} = \sin\varphi\sin\delta + \cos\varphi\cos\delta\cos\omega_{t},\tag{3}$$

$$\omega_{\rm t} = \frac{15\pi(t - 12)}{180},\tag{4}$$

$$\delta = -\varphi_r \cos \frac{360\pi (d+10)}{365 \times 180},\tag{5}$$

where  $\varphi$  is the latitude (positive north), rad,  $\varphi_r$  is the latitude of the Tropic of Cancer, rad, t is the time in hours, and d represents the number of days counted from January 1. The normalized shadow  $l_s$  can be calculated using Eq. (6).

$$l_{s} = \begin{cases} h \tan \theta_{z} \sin \theta & l_{s} < w \\ w & l_{s} \ge w \end{cases}$$
 (6)

where  $\theta = \theta_{az} - \theta_C$ , and h and w denote the normalized building height and canyon width, respectively. The sky view factors are defined as follows:

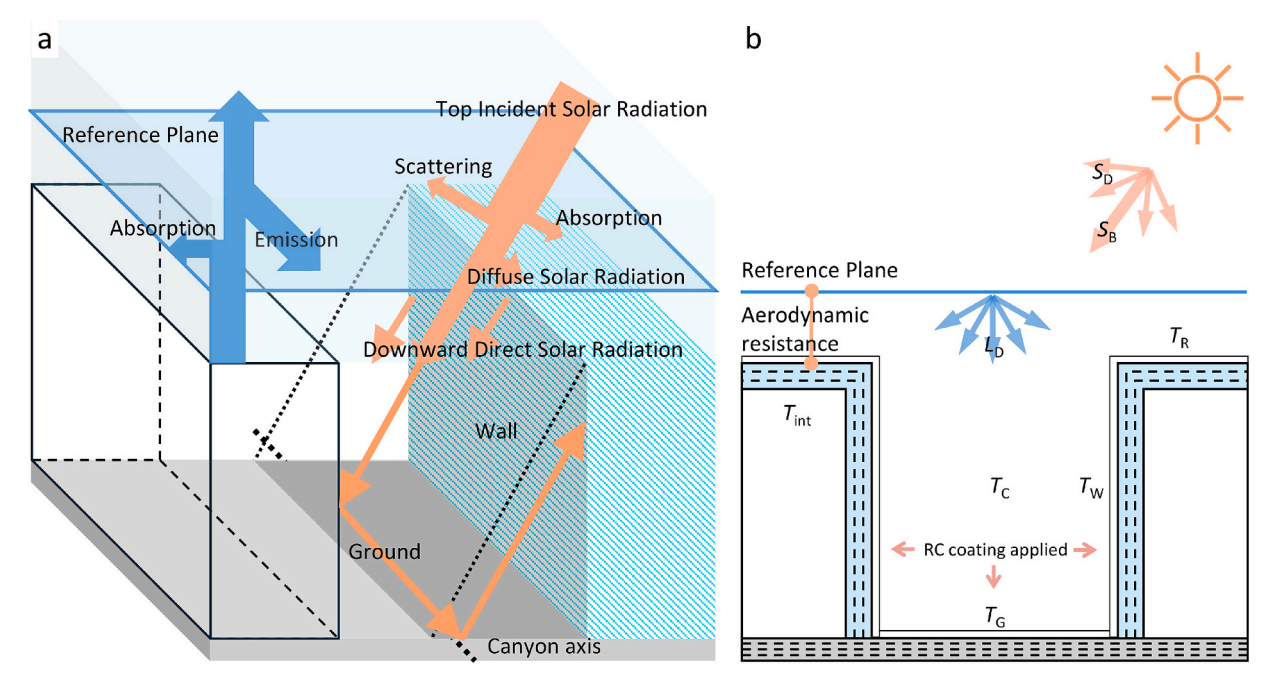


Fig. 1. Numerical Model. (a) Schematic of the UCM, including shading, solar radiation, and longwave radiation. (b) Variables in the UCM, where the entire street is assumed to be covered with RC coatings.

$$F_{\rm SG} = F_{\rm GS} = \sqrt{1 + \left(\frac{h}{w}\right)^2} - \frac{h}{w},\tag{7}$$

$$F_{\text{WW}} = \sqrt{1 + \left(\frac{w}{h}\right)^2} - \frac{w}{h},\tag{8}$$

$$F_{\rm GW} = 0.5(1 - F_{\rm GS}),\tag{9}$$

$$F_{WG} = F_{WS} = 0.5(1 - F_{WW}), \tag{10}$$

where the subscripts S, R, W, G denote sky, roof, wall, and ground, respectively.

For convective heat transfer within the urban canyon, the height-dependent mean wind speed  $\langle \overline{u}(z) \rangle$ , m·s<sup>-1</sup>, is defined by Eq. (11) [41].

$$\langle \overline{u}(z) \rangle = \frac{u_*}{\kappa} \ln \left( \frac{z - d_T}{z_{0T}} \right),$$
 (11)

where  $\kappa$  is the von Karman constant, taking a value of 0.4 [42],  $u^*$  is the friction velocity,  $\text{m·s}^{-1}$ ,  $d_T$  is the displacement height, m,  $z_{OT}$  is the effective roughness length, m. The wind speed at the reference level  $z_{\text{Ref}} = 2H$ , is shown in Eq. (12).

$$\langle \overline{u}(\mathbf{z}_{Ref}) \rangle = \frac{u_*}{\kappa} \ln\left(\frac{2H - d_T}{\mathbf{z}_{0T}}\right).$$
 (12)

The wind speed at the roof  $u_R$  is provided in Eq. (13), while the aerodynamic resistance is shown in Eq. (14).

$$\frac{u_{\rm R}}{\langle \overline{u}(z_{\rm Ref}) \rangle} = \ln\left(\frac{H + \delta_{\rm R} - d_{\rm T}}{z_{0T}}\right) / \ln\left(\frac{z_{\rm Ref} - d_{\rm T}}{z_{0T}}\right),\tag{13}$$

$$R_{\rm R} = \ln\left(\frac{\delta_{\rm R}}{z_{\rm m,R}}\right) \ln\left(\frac{\delta_{\rm R}}{z_{\rm h,R}}\right) / \kappa^2 u_{\rm R} + \frac{\langle \overline{u}(z_{\rm Ref}) \rangle - u_{\rm R}}{u_*^2},\tag{14}$$

where  $\delta_{\rm R}$  is the thickness of the internal boundary layer, m, H is the building height, m,  $u^{}_{\rm r}$  is the friction velocity, m·s $^{-1}$ ,  $z_{\rm m,R}$  is the roof momentum roughness length, m,  $z_{\rm h,R}$ , is the roof heat roughness length, m.

The canyon wind speed  $u_C$  is estimated at half the height of the

canyon [43]. The equation is shown in Eq. (15). The aerodynamic resistance is shown in Eq. (16),

$$u_{\rm C} = \frac{2}{\pi} \exp\left(-\frac{1}{4} \frac{h}{w}\right) u_{\rm R},\tag{15}$$

$$R_{\rm C} = \ln \left( \frac{\delta_{\rm C}}{z_{\rm m,C}} \right) \ln \left( \frac{\delta_{\rm C}}{z_{\rm h,C}} \right) / \kappa^2 u_{\rm C} + \frac{\langle \overline{u}(z_{\rm Ref}) \rangle - u_{\rm C}}{u_*^2}. \tag{16}$$

The conductive heat fluxes through the roof, walls, and ground are analyzed using a one-dimensional unsteady heat conduction equation. The governing equation is provided in Eq. (17) and Eq. (18), with boundary conditions specified in Eq. (19) and Eq. (20), respectively. The ground is assumed to be adiabatic at infinity.

$$\rho c_{p} \frac{\partial T}{\partial t} = \frac{\partial}{\partial x} \left[ \lambda \frac{\partial T}{\partial x} \right], \tag{17}$$

$$\frac{T(x,t+1) - T(x,t)}{\Delta t} = a \frac{T(x+1,t) - 2T(x,t) + T(x-1,t)}{\Delta x^2},$$
 (18)

$$x = 0$$
,  $\frac{\partial T}{\partial x} = R_n - Q_H - Q_{LE}$ ,  $x = d$ ,  $T = T_{indoor}$ , (19)

$$x = 0$$
,  $\frac{\partial T}{\partial x} = R_n - Q_H - Q_{LE}$ ,  $x = \infty$ ,  $\frac{\partial T}{\partial x} = 0$ . (20)

#### 2.1.2. Radiative cooling model

The RC model integrated with the UCM needs to account for the tworeflection model used in the UCM. In the UCM model, the radiative terms are described by Eq. (21) [40]. The general energy balance equation for the RC model is given in Eq. (22) [44].

$$R_{\rm n} = S_{\downarrow} + L_{\downarrow} - S_{\uparrow} - L_{\uparrow},\tag{21}$$

$$q_{\rm cool} = q_{\rm emi}(T) - q_{\rm atm}(T_{\rm amb}) - q_{\rm sun}(T) - q_{\rm c}, \tag{22}$$

where S and L denote shortwave and longwave radiation, respectively,  $W \cdot m^{-2}$ , down and up arrows indicate the incoming and outgoing components, respectively.  $q_{\rm emi}$  is the outward radiative emission,  $W \cdot m^{-2}$ .  $q_{\rm atm}(T_{\rm amb})$  denotes the atmospheric radiation at temperature  $T_{\rm amb}$ ,

W·m<sup>-2</sup>.  $q_{\text{sun}}$  represents the absorbed solar radiation, W·m<sup>-2</sup>; and  $q_{\text{c}}$  refers to the conductive and convective heat exchange with the environment, W·m<sup>-2</sup>. Therefore, by combining Eqs. (1), (21), and (22), the energy balance equation can be rewritten as Eq. (23),

$$q_{\text{sun}}(T) + q_{\text{atm}}(T_{\text{amb}}) - q_{\text{emi}}(T) = Q_{\text{H}} + Q_{\text{LE}} + Q_{\text{G}}.$$
 (23)

In the UCM, the two-reflection model is employed to account for radiation reflections from three components: direct and diffuse solar radiation ( $S_B$  and  $S_D$ ), longwave radiation from the atmosphere ( $L_1$ ), and longwave radiation emitted by surfaces  $(L_{\uparrow})$ . These components correspond to  $q_{\text{sun}}$ ,  $q_{\text{atm}}$ , and  $q_{\text{emi}}$  in the RC model, respectively. To accurately simulate the cooling performance of RC coatings in urban street canyons, the model has been modified from the traditional UCM [40] by addressing each component individually. Shaded and unshaded areas are treated differently by considering  $S_B$  and  $S_D$ . When handling surface multiple reflections,  $S_{\rm B}$  is addressed using the zenith angle, defined as the ratio of shadow length to building height. Meanwhile,  $S_{\mathrm{D}}$ ,  $q_{\mathrm{atm}}$ , and  $q_{\rm emi}$  are modeled using sky view factors, incorporating interactions between walls and walls, and between walls and the ground. By integrating these factors, the modified model provides a more precise representation of urban street canvons with RC coatings. For clarity, the detailed radiation reflection process is illustrated in Fig. 2. Both direct and diffuse radiation are represented as arrows to simplify visualization. The impact of these radiative processes is further elaborated as follows:

$$q_{\text{sun}} = \frac{S}{1000} \int_{0}^{\infty} I_{\text{AM1.5}}(\lambda) \varepsilon_{\text{RC}}(\lambda) d\lambda, \tag{24}$$

$$\overline{a}_{\rm RC} = 1 - \frac{\int_0^\infty I_{\rm AM1.5}(\lambda) \varepsilon_{\rm RC}(\lambda) d\lambda}{1000},\tag{25}$$

$$S_{R} = (1 - \overline{a}_{RC})(S_{B} + S_{D}), \tag{26}$$

$$S_{\rm w} = (1 - \overline{a}_{\rm RC}) \begin{pmatrix} S_{\rm B} \frac{l_{\rm S}}{2h} + S_{\rm D} F_{\rm WS} + \\ \overline{a}_{\rm RC} S_{\rm B} \frac{l_{\rm S}}{2h} F_{\rm WW} + \overline{a}_{\rm RC} S_{\rm D} F_{\rm WS} F_{\rm WW} + \\ \overline{a}_{\rm RC} S_{\rm B} \frac{w - l_{\rm S}}{w} F_{\rm WG} + \overline{a}_{\rm RC} S_{\rm D} F_{\rm GS} F_{\rm WG} \end{pmatrix}, \tag{27}$$

$$S_{\rm G} = (1 - \overline{a}_{\rm RC}) \begin{pmatrix} S_{\rm B} \frac{w - l_{\rm S}}{w} + S_{\rm D} F_{\rm GS} + \\ \overline{a}_{\rm RC} S_{\rm B} \frac{l_{\rm S}}{2h} F_{\rm GW} + \overline{a}_{\rm RC} S_{\rm D} F_{\rm WS} F_{\rm GW} \end{pmatrix}, \tag{28}$$

where  $S_{\rm B}$  is the direct solar radiation received by a horizontal surface, W·m<sup>-2</sup>,  $S_{\rm D}$  is the diffuse solar radiation received by a horizontal surface, W·m<sup>-2</sup>, and a is the surface albedo.

The longwave radiation can be computed as follows:

$$q_{\rm atm}(T_{\rm amb}) = \int_0^\infty \int_0^{2\pi} I_{\rm BB}(T_{\rm amb},\lambda) \varepsilon(\lambda) \varepsilon_{\rm atm}(\lambda,\theta) {\rm cos} \theta {\rm d}\Omega {\rm d}\lambda, \tag{29} \label{eq:29}$$

$$q_{\rm atm}(T_{\rm amb}) = \int_0^\infty I_{\rm BB}(T_{\rm amb},\lambda) \varepsilon(\lambda) \int_0^{2\pi} \int_0^{\pi/2} \varepsilon_{\rm atm}(\lambda,\theta) {\rm cos} \theta {\rm sin} \theta {\rm d} \theta {\rm d} \varphi {\rm d} \lambda, \tag{30}$$

$$q_{\mathrm{emi}}(T) = \int_{0}^{\infty} \int I_{\mathrm{BB}}(T,\lambda)\varepsilon(\lambda,\theta)\mathrm{cos}\theta\mathrm{d}\Omega\mathrm{d}\lambda,$$
 (31)

$$L_{\rm R} = \overline{\varepsilon}_{\rm R} q_{\rm atm}(T_{\rm amb}) - q_{\rm emi}(T_{\rm R}), \tag{32}$$

$$L_{W} = \overline{\varepsilon}_{W}(q_{atm}(T_{amb})F_{WS} + q_{emi}(T_{G})F_{WG} + q_{emi}(T_{W})F_{WW}) + \overline{\varepsilon}_{W}(1 - \overline{\varepsilon}_{G})q_{atm}(T_{amb})F_{GS}F_{WG} + \overline{\varepsilon}_{W}(1 - \overline{\varepsilon}_{W})q_{atm}(T_{amb})F_{WS}F_{WW} + \overline{\varepsilon}_{W}(1 - \overline{\varepsilon}_{W})q_{emi}(T_{W})F_{WW}F_{WW} + 2(1 - \overline{\varepsilon}_{G})q_{emi}(T_{W})F_{GW}F_{WG} + (1 - \overline{\varepsilon}_{W})q_{emi}(T_{G})F_{WG}F_{WW} - q_{emi}(T_{W})$$

$$(33)$$

$$L_{G} = \overline{\varepsilon}_{G}(q_{\text{atm}}(T_{\text{amb}})F_{\text{GS}} + 2q_{\text{emi}}(T_{W})F_{\text{GW}}) - q_{\text{emi}}(T_{G}) + 2\overline{\varepsilon}_{G}(1 - \overline{\varepsilon}_{W})q_{\text{atm}}(T_{\text{amb}})F_{WS}F_{\text{GW}} + (1 - \overline{\varepsilon}_{W})q_{\text{emi}}(T_{G})F_{GW}F_{WG} + 2\overline{\varepsilon}_{G}(1 - \overline{\varepsilon}_{W})q_{\text{emi}}(T_{W})F_{WW}F_{GW}$$

$$(34)$$

where  $\varepsilon$  is the emissivity and T the surface temperature, K. The subscripts S, R, W, G denote sky, roof, wall, and ground, respectively.

#### 2.2. Canyon parameters

Different urban configurations and coating strategies directly influence the effectiveness of RC in mitigating UHI effects. To explore the optimal application of RC across diverse urban environments, the simulation extends the use of coatings from rooftops to walls and ground surfaces, while considering various urban and street configurations.

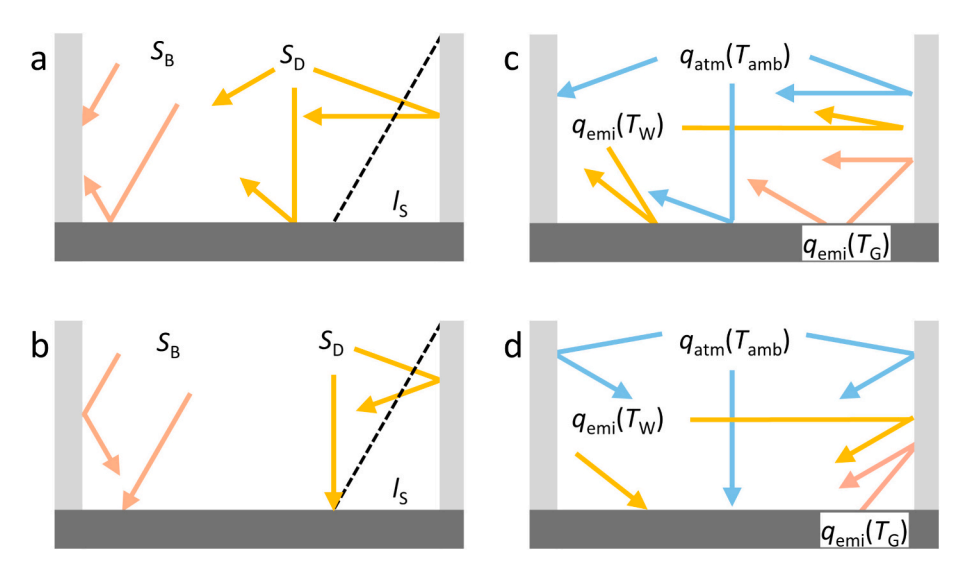


Fig. 2. Schematic diagram of the radiative reflection in the two-reflection model. (a) Solar radiation received by the wall. (b) Solar radiation received by the ground. (c) Longwave radiation received by the ground.

**Table 1** Input canyon surface parameters.

Parameters	Units	Symbols	Values
Reference height of atmospheric measurements	m		10
Urban canyon aspect ratio			0.5-2
Urban canyon orientation	۰		−180 - 180
Thickness of roof	m	$d_{ m R}$	0.5
Thickness of wall	m	$d_{W}$	0.3
Thermal conductivity of roof	$W \cdot K^{-1} \cdot m^{-1}$	$k_{ m R}$	1.0
Thermal conductivity of wall	$W \cdot K^{-1} \cdot m^{-1}$	$k_{\mathrm{W}}$	1.3
Thermal conductivity of ground	$W \cdot K^{-1} \cdot m^{-1}$	$k_{ m G}$	1.2
Heat capacity of roof	$MJ\cdot K^{-1}\cdot m^{-3}$	$c_{ m R}$	2.0
Heat capacity of wall	$MJ\cdot K^{-1}\cdot m^{-3}$	$c_{\mathrm{W}}$	1.2
Heat capacity of ground	$MJ\cdot K^{-1}\cdot m^{-3}$	$c_{ m G}$	1.0
Roof momentum roughness length	m	$z_{ m m,R}$	0.01
Roof heat roughness length	m	$z_{\rm h,R}$	0.001
Canyon momentum roughness length	m	$z_{ m m,C}$	0.05
Canyon heat roughness length	m	$z_{ m h,C}$	0.005

Table 1 and Table 2 provide detailed information on urban structural parameters and the geographical locations of different cities, respectively. Specifically, Table 1 outlines the various structural parameters pertinent to urban canyon. Table 2 details the geographical locations of the cities under study, including latitude and longitude.

#### 2.3. Weather data

The input weather parameters were obtained from the fifth generation of the European Centre for Medium-Range Weather Forecasts (ECMWF) atmospheric re-analysis for global climate [45] (ERA5). Produced by the Copernicus Climate Change Service (C3S) at ECMWF, ERA5 provides data with a spatial resolution of 0.25°. The simulation spanned a period of 8760 h, starting at 08:00 on January 1, 2023 (UTC  $\pm$  8). Table 3 provides an overview of the data sources used in the simulation, among which the reanalysis data are accumulated over a 1-h period and are expressed in joules per square meter (J·m $^{-2}$ ). To convert these values to watts per square meter (W·m $^{-2}$ ), the accumulated values must be divided by the accumulation period in seconds.

#### 3. Model validation

In this study, the model validation is divided into two parts: the validation of the RC model and the validation of the UCM. This separation is due to the absence of cases where RC coatings are applied to walls that are shaded by surrounding structures. The validation of the RC roof can verify the equivalent solar emissivity and the hemispherical integration of longwave radiation, both of which are integrated into the UCM for roofs, walls, and ground. Subsequently, the validation of rooftop and ground surface temperatures within the UCM can confirm the angular dependence of atmospheric emissivity for walls and ground within the urban canyon. This is addressed in the model by incorporating the sky view factor multiplied by atmospheric radiation. Since ground temperature is also influenced by radiation emitted from walls,

Table 2
Different city coordinates.

Cities	Locations		Cities	Locations	
Urumqi	87.58°E	43.82°N	Hong Kong	114.18°E	22.33°N
Lhasa	91.13°E	29.66°N	Wuhan	114.32°E	30.52°N
Xining	101.77°E	36.62°N	Beijing	116.40°E	39.91°N
Kunming	102.71°E	25.04°N	Hangzhou	120.20°E	30.27°N
Chongqing	106.50°E	29.55°N	Shanghai	121.45°E	31.23°N
Xi'an	108.95°E	34.27°N	Taipei	121.50°E	25.04°N
Sanya	109.50°E	18.26°N	Harbin	126.63°E	45.75°N
Guangzhou	113.25°E	$23.12^{\circ}N$			

**Table 3** Input parameters from ERA5.

Symbols	Full name	Units
u10	10 m U wind component	$m \cdot s^{-1}$
v10	10 m V wind component	$m \cdot s^{-1}$
fdir	Total sky direct solar radiation at a surface	$J \cdot m^{-2}$
ssrd	Surface short-wave radiation downwards	$J \cdot m^{-2}$
strd	Surface long-wave radiation downwards	$J \cdot m^{-2}$
t2m	2 m temperature	K

its validation can indirectly confirm the accuracy of wall simulations. Therefore, a two-step validation process has been conducted. First, a rooftop experiment using radiative cooling coatings is performed to validate the integration of the radiative cooling mechanism into the UCM. Second, the UCM is validated against experimental data from the literature for scenarios without radiative cooling, focusing on rooftop and ground surface temperatures. This step verifies the feasibility of using the sky view factor to handle atmospheric radiation and indirectly validates the accuracy of wall simulations. The details of the validation process are shown in Fig. 3.

To verify the reliability of the coupled UCM numerical model and assess the cooling effectiveness of the coating, an experiment was conducted at the Tong Fuk Correctional Institution in Hong Kong, as shown in Fig. 3. For model validation, a RC coating was applied to the roof surface of the building. This coating is commercially available and suitable for large-scale application. It consists of two main components: a polymer matrix with high emissivity in the atmospheric window (8-13 µm) and spherical particles with high solar reflectivity. The reflectance spectrum of this coating is shown in Fig. 4, Sample 1. The experimental setup, depicted in Fig. 3a, involved two buildings; Block A. where the RC coating was applied to the roof to test its cooling performance (specific coating details are shown in Fig. 3b, and Block J, which remained untreated and served as the control unit). Comprehensive field tests were conducted to provide a rigorous comparison between the treated and untreated buildings. Resistance temperature detectors (Pt100) were employed in different places to monitor temperatures, as illustrated in Fig. 3c. At each position, measurements included the indoor air temperature, the indoor ceiling surface temperature, and the outdoor roof surface temperature. A weather station (DAVIS Vantage Pro2 Plus) measured local meteorological parameters, including wind speed and direction, ambient temperature, and solar radiation, with data recorded every 5 min. A data logger (GRAPHTEC GL840) was used to record various variables at 1-min intervals. The accuracy of each measurement is detailed in Table 4.

During the field test study, the environmental variables collected, including air temperature, direct solar radiation, indoor temperature, and wind speed, were used as model inputs, along with the spectral characteristics of Sample 1. The experiment commenced at 12:00 on November 8, 2023, and lasted for 100 h. Fig. 3d illustrates the temperature variations of the coated and uncoated roof separately. The model predictions align closely with the experimental outcomes for both coated and uncoated roofs, accurately capturing the timing and amplitude of peak roof temperatures. Fig. 3e shows the satellite image of the experiment from the literature, with weather data downloaded through ERA5. The comparison between the experimental data and the simulated results is presented in Fig. 3f. It can be seen that both the rooftop and ground temperatures closely match the experimental data, demonstrating that the two-reflection model accurately simulates ground temperature.

Furthermore, a more detailed quantitative analysis is conducted using the coefficient of variation of the root-mean-square error (CV [RMSE]) and the normalized mean bias error (NMBE) from ASHRAE Guideline 14–2014. as defined in eqs. (35) and (36).

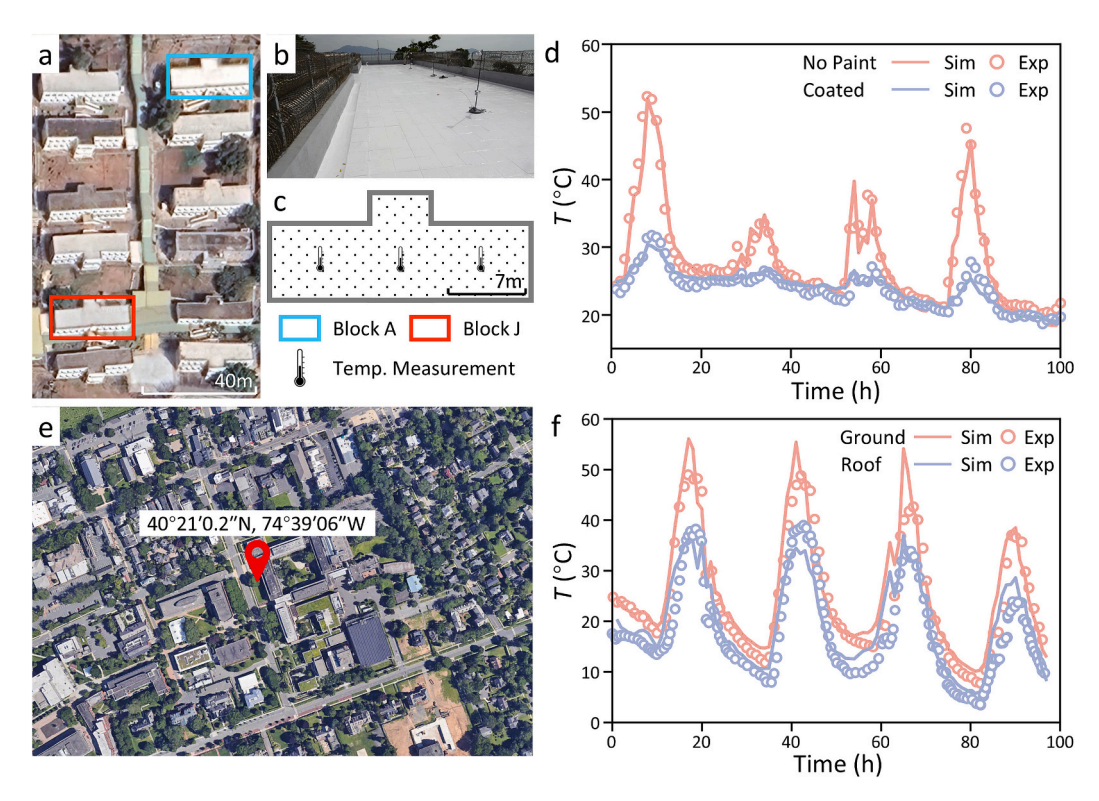


Fig. 3. Experimental setup and model validation result. (a) Satellite image of the experimental setup at the Tong Fuk Correctional Institution in Hong Kong. (b) Photograph of the rooftop after the application of the RC coating. (c) Schematic diagram of the distribution of temperature measurement points on the rooftop. (d) Comparison of experimental data and simulated results for the coated and uncoated roofs over the experimental period. (e) Satellite image of the experimental setup from the literature. (f) Comparison of simulated results with experimental data from the literature.

$$CV(RMSE) = \frac{\sqrt{\sum_{(n-\bar{y})^2} (y_i - \bar{y})^2}}{\bar{y}},$$
(35)

$$NMBE = \frac{\sum_{u=1}^{n} (y_i - \widehat{y}_i)}{(n-p) \times \overline{y}},$$
(36)

where  $\widehat{y}$  is simulation predicted data,  $y_i$  is utility data. For the RC model validation, the CV[RMSE] between the model and experimental results for uncoated and coated roofs were 7.13 % and 4.18 %, respectively, while the NMBE ranged from 4.94 % to 3.26 %. Similarly, For the UCM validation, the CV[RMSE] between the model and experimental results for ground and roof temperatures were 6.99 % and 4.23 %, respectively, with NMBE values ranging from 4.84 % to 3.30 %. These results demonstrate that the model predictions are sufficiently accurate.

#### 4. Results and discussion

#### 4.1. Surface temperature changes with various coatings

To investigate how coatings with varying spectral properties can mitigate the UHI effect, a comparative study is conducted with five distinct coatings [25–28]. These materials, classified as films and paints, offer potential for large-scale fabrication and are suitable for application to building exteriors. Sample 1 is a commercial coating, Sample 2 is a multilayer film comprising seven layers [25] (SiO<sub>2</sub>, HfO2, and Si, etc.), Sample 3 is a composite of resonant polar dielectric microspheres embedded randomly within a polymeric matrix [26], Sample 4 is a hierarchically porous coating made from polymer [27], Sample 5 is a glass-polymer hybrid thin film [28]. The specific spectral characteristics of each material are illustrated in Fig. 4a. A comparison of their spectral properties indicates that Sample 2 exhibits the highest solar reflectance in the solar spectrum (0.25–2.5  $\mu$ m) but the lowest emissivity in the

atmospheric window. In contrast, Samples 1, 3, and 4 show high emissivity in the atmospheric window, though their solar reflectance is not as high as that of Sample 2.

In this study, the wall temperature is defined as the average surface temperature of the building facades on both sides of the street within the urban canyon, incorporating the contributions of both shaded and sunlit walls. The ground temperature represents the mean surface temperature of the ground in the canyon, with the model assuming uniformity of the ground temperature at a small spatial scale. Lastly, the canyon temperature is characterized as the air temperature within the street canyon, reflecting the thermal interactions between the walls, ground, and surrounding air. Fig. 4b illustrates the hourly temperature reductions in rooftop, wall, ground, and canyon achieved by applying RC coatings to canyon surfaces in 2023 in Hong Kong. The temperature reduction curves for all coatings exhibit similar trends. Notably, the cooling effects on rooftops and ground surfaces are comparable, as are those on walls within urban canyons. This similarity is primarily attributed to the orientation of these surfaces; upward-facing rooftops and ground surfaces fully exploit the cooling potential of RC coatings. Additionally, the cooling effectiveness of these coatings diminishes significantly at night, when only the atmospheric window contributes to cooling. In contrast, during daylight hours, the reflection of solar radiation markedly enhances the cooling efficiency. The analysis of the different coatings indicates that Sample 2 exhibits the highest potential for surface temperature reduction, followed sequentially by Samples 5, 4, and 3, with Sample 1 being the least effective. Quantitatively, Sample 2 can reduce ground temperatures by up to 35.2 °C, with an average daily cooling effect of approximately 13.1 °C. In comparison, the average daily cooling effects for Samples 1, 3, 4, and 5 are 8.6 °C, 10.3 °C, 10.0 °C, and 12.1 °C, respectively. Both the comparative analysis between samples and the examination of diurnal cooling effects within the same sample suggest that solar reflectance significantly influences the cooling capacity of the coatings, whereas emissivity in the

Z. Li et al. Applied Energy 393 (2025) 126138

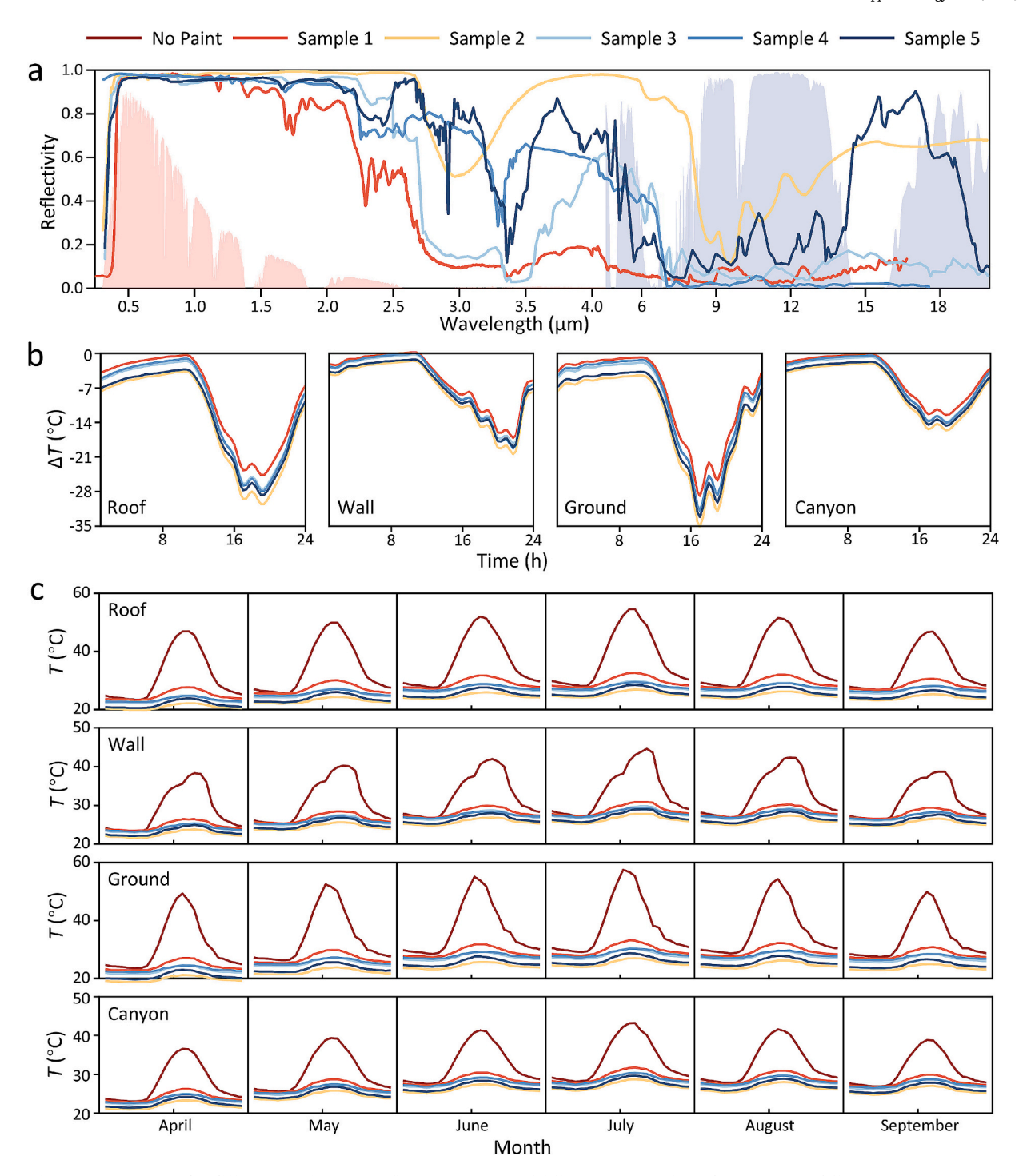


Fig. 4. Surface temperature under different coatings. (a) Reflectivity spectrum of different coatings. (b) Daily temperature difference curves compared with that of no paint. (c) Average monthly temperature curves compared with that of no paint.

**Table 4**Measurement accuracy of parameters.

Parameters	Measurement range	Accuracy
Surface Temperature	−50 °C to +150 °C	±0.5 °C
Outside Temperature	$-40~^{\circ}\text{C}$ to $+65~^{\circ}\text{C}$	±0.3 °C
Dewpoint Temperature	−76 °C to +65 °C	±1 °C
Wind Speed	0 to 89 m·s <sup>-1</sup>	$\pm 0.9~\text{m}\cdot\text{s}^{-1}$
Solar Radiation	0 to 1800 W·m $^{-2}$	$\pm 5$ % of full scale

atmospheric window plays a comparatively smaller role. Fig. 4c presents the monthly average temperature profiles from April to September, comparing uncoated surfaces to those treated with various coatings. During the hottest months of the year, these coatings exhibit substantial potential in mitigating the UHI effect. The cooling effects are most pronounced from June to August, with rooftop and ground surface temperatures reduced by 19–24  $^{\circ}\text{C}$  during midday peak temperatures, and wall and urban canyon temperatures decreasing by approximately 8–11  $^{\circ}\text{C}$ . Notably, Sample 2 consistently demonstrates the lowest temperature profiles compared to the other samples. Therefore, when considering the application of coatings on complex surfaces, such as

concrete buildings or asphalt pavements, it is recommended to prioritize materials with higher reflectance in the solar spectrum and subsequently consider their emissivity in the atmospheric window range.

#### 4.2. RC efficiency in various urban configurations

The application of RC materials significantly influences their effectiveness. Shading can diminish their performance within the solar spectrum, and when RC coatings are applied to vertical surfaces, the energy emitted may be absorbed by adjacent walls or the ground [44].

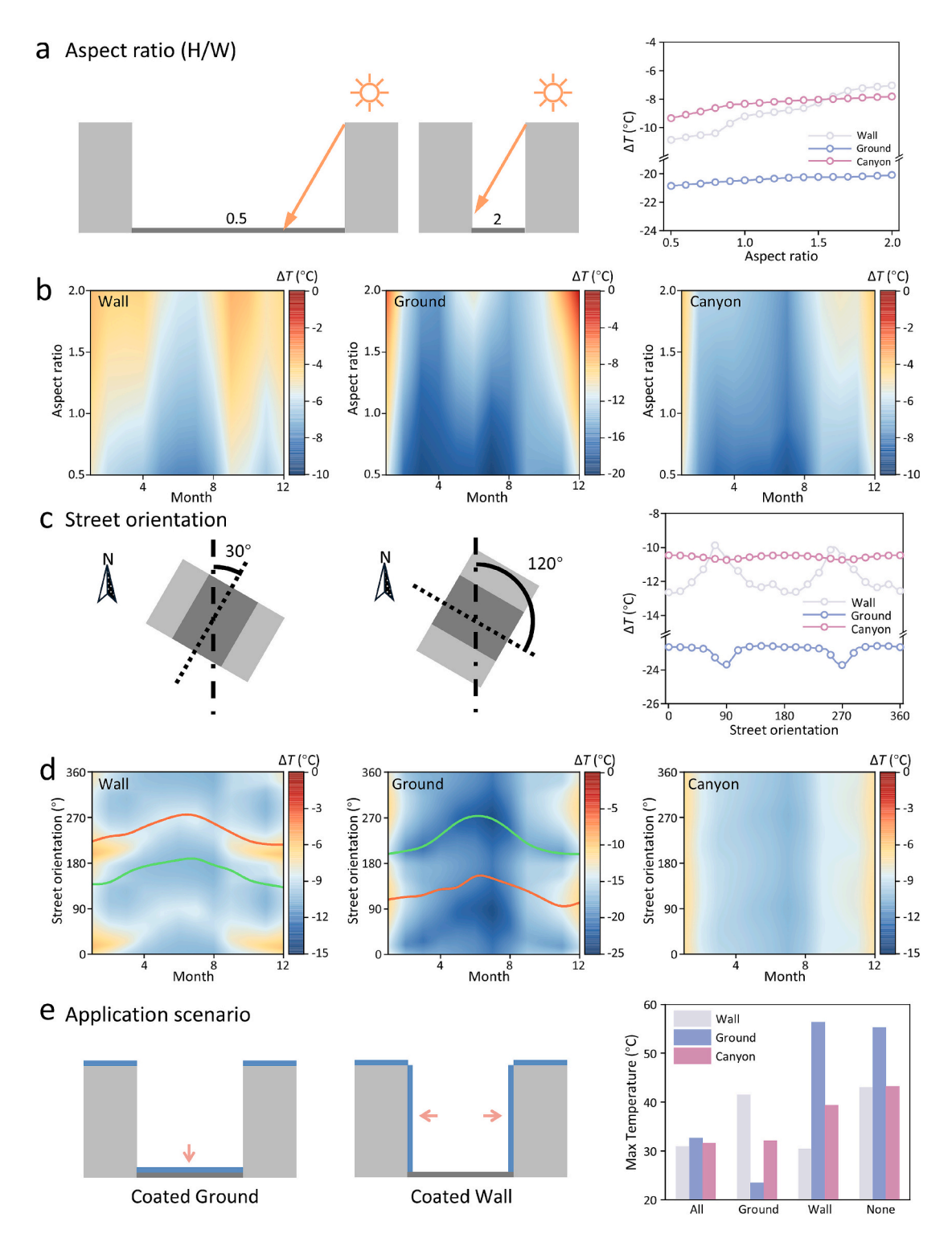


Fig. 5. Cooling effects of different urban canyon configurations. (a) Temperature differences as a function of aspect ratio in August 2023 in Hong Kong. (b) Average monthly temperature differences under different aspect ratios throughout the year, comparing scenarios with and without RC coatings. (c) Temperature differences as a function of street orientation in August 2023 in Hong Kong. (d) Average monthly temperature differences for different street orientations over the year, with and without RC coatings. (e) Maximum surface temperatures under different coating scenarios on the hottest day of the year, comparing the effects of applying RC coatings to walls, ground surfaces, or both.

Consequently, the geometric characteristics of urban environments, such as building height, street width, and street orientation, play a crucial role in the radiative exchange and distribution between surfaces within urban canyons, thereby affecting the performance of RC coatings. Additionally, the placement of RC coatings (on walls, ground, or both) significantly influences their effectiveness. For example, a RC-coated wall will reflect more solar radiation and emit additional infrared wavelength radiation, which will increase the surface temperature of adjacent walls. Fig. 5 illustrates the relationship between temperature differences and various urban canyon configurations in Hong Kong in 2023.

#### 4.2.1. Aspect ratio

To optimize the application of RC coatings across various urban geometries, the simulation was conducted considering aspect ratios ranging from 0.5 to 2, representing wider to narrower streets, and evaluated coatings applied to both walls and ground surfaces. Fig. 5b presents the monthly average temperature difference of walls, ground, and canyons across different aspect ratios throughout the year. These findings indicate that cooling effectiveness generally decreases as the aspect ratio increases. Specifically, higher aspect ratios, associated with taller buildings and narrower streets, lead to increased shading and reduced solar radiation on surfaces, thereby diminishing the cooling efficiency of the RC coatings. The curves in Fig. 5a exemplify this trend for Hong Kong during August, demonstrating a consistent decline in cooling effectiveness across walls, ground, and canyons as the aspect ratio increases. Overall, RC coatings are most effective at lower aspect ratios, where cooling efficiency is the highest. However, as the aspect ratio increases (with building height significantly exceeding street width), the cooling performance diminishes and stabilizes at constant values of -6 °C for walls, -20 °C for ground, and -8 °C for urban canyons, respectively. Despite the decrease, RC coatings exhibit significant cooling effects across all aspect ratios. To maximize costeffectiveness, applying RC coatings to both walls and ground surfaces in low-density or low-rise urban areas is recommended, where the cooling benefits are substantial and lead to considerable temperature reductions. In contrast, for deep urban canyons with higher aspect ratios, it is advisable to prioritize RC coatings on walls, as shading from tall buildings diminishes the effectiveness of ground coatings. Additionally, applying RC surfaces to the walls of taller buildings or the roofs of shorter structures within a heterogeneous urban landscape may further enhance cooling effectiveness by exploiting the variability in building heights.

#### 4.2.2. Street orientation

Solar radiation incident on urban surfaces varies with street orientation and time of day. To effectively utilize the cooling capacity of RC coatings under different spatial and temporal distributions of solar radiation, the cooling effect for street orientations ranging from 0° to 360° was simulated. Fig. 5d presents the impact of various street orientations on the monthly average temperature differences of walls, grounds, and canyons. The maximum temperature reduction varies with orientation due to differences in incident solar radiation. Specifically, Fig. 5c shows the temperature reduction in Hong Kong in August at different orientations, incident solar radiation on walls ranges from 300 W·m<sup>-2</sup> at orientations of 70° or 260°, up to 450 W·m<sup>-2</sup> at orientations of 160° or 340°. In contrast, ground surfaces consistently receive high solar radiation, with a minimum of 750 W·m<sup>-2</sup> at orientations of 160° or 340°, and a maximum of 770  $W \cdot m^{-2}$  at orientations of 70° or 260°. This trend varies with the month, as can be seen from the maximum and minimum temperature reduction curves highlighted in Fig. 5d. To maximize the cooling benefits of RC coatings, it is advisable to prioritize application on wall surfaces oriented southeast, while for ground surfaces, northeast orientations are preferred. These orientations receive the highest solar radiation, optimizing the cooling effectiveness of the coatings. Additionally, this recommendation is based on Hong Kong, for cities located

at higher latitudes, the advisable street orientations will rotate counterclockwise accordingly.

#### 4.2.3. Different painting scenarios

The effectiveness of RC coating is also influenced by different application scenarios, particularly due to their significant reflection of solar radiation. This reflected radiation can interact with other RCcoated surfaces, affecting the net amount of solar radiation each surface receives. To investigate this effect, streets with various coating schemes were simulated. Fig. 5e shows the street temperatures for different configurations on the hottest summer day. Coating only the walls or only the ground surface yields the greatest cooling effect on these respective surfaces, reducing temperatures by 30 °C and 24 °C, respectively. However, when both walls and ground are coated, the temperatures increase by 1 °C on the walls and 9 °C on the ground compared to coating the walls or ground alone. Therefore, for maximum cooling efficiency, applying RC coatings solely to ground surfaces is effective in wider streets with lower buildings, while in narrow streets with taller buildings, wall coatings are more beneficial to maximize building cooling and energy savings. Additionally, RC coatings may cause glare, potentially affecting pedestrians in broad streets, and thus, specific applications should consider local conditions and urban design

Based on the above analysis, to maximize the cooling effectiveness of RC coatings, coating ground surfaces in wider streets oriented northeast was recommended, while in narrower streets, priority should be given to coating the walls on both sides of streets oriented southeast. While in regions, such as Hong Kong, where there is an urgent need to reduce building energy consumption, it is advisable to apply RC coatings to both walls and ground surfaces. Considering the potential glare issue, the use of colored RC coatings is recommended to mitigate its impact. This strategic application fully leverages the optimal solar radiation exposure for each surface, enhancing the overall performance of RC coatings. It is important to adjust these recommendations based on the city's latitude; for cities located at higher latitudes than Hong Kong, the recommended street orientations will rotate counterclockwise accordingly due to changes in cumulative solar radiation caused by latitude.

## 4.3. Maximum surface temperature reduction of RC coatings across China

The performance of RC coatings is critically influenced by climatic conditions such as solar radiation, sunlight duration, and cloud cover, in addition to urban canyon configurations. In China, variations in altitude, geographical location, and regional characteristics [46] lead to complex climatic profiles. To assess the applicability of RC coatings across China's diverse climatic conditions, the ERA5 weather data [45] was utilized to conduct comprehensive simulations of RC-coated streets in 338 Chinese cities for the year of 2023. The ERA5 meteorological data, providing hourly observations of infrared wavelength radiation and solar radiation, wind speed, and air temperature over the course of a year, effectively reflects the different climates of these cities resulting from geographical disparities. The spectrum of Sample 2 was used for these simulations, as it demonstrated superior performance in previous analyses. The results of this analysis are presented in Fig. 6, which evaluates the maximum temperature reductions over one year compared with uncoated streets. Additionally, Fig. 6a provides detailed temperature profiles for six representative cities selected from different climate zones across China.

This study highlights that the northern and north-western regions of China, classified as severe cold and cold zones in the country's building climate classification, exhibit the highest cooling potential for RC coatings. This is primarily due to extended solar exposure and intense solar radiation in these areas. For instance, north-western regions like Lhasa, situated at a high altitude and a relatively low latitude, receive substantial solar radiation. Similarly, Urumqi, located in arid zones,

Z. Li et al. Applied Energy 393 (2025) 126138

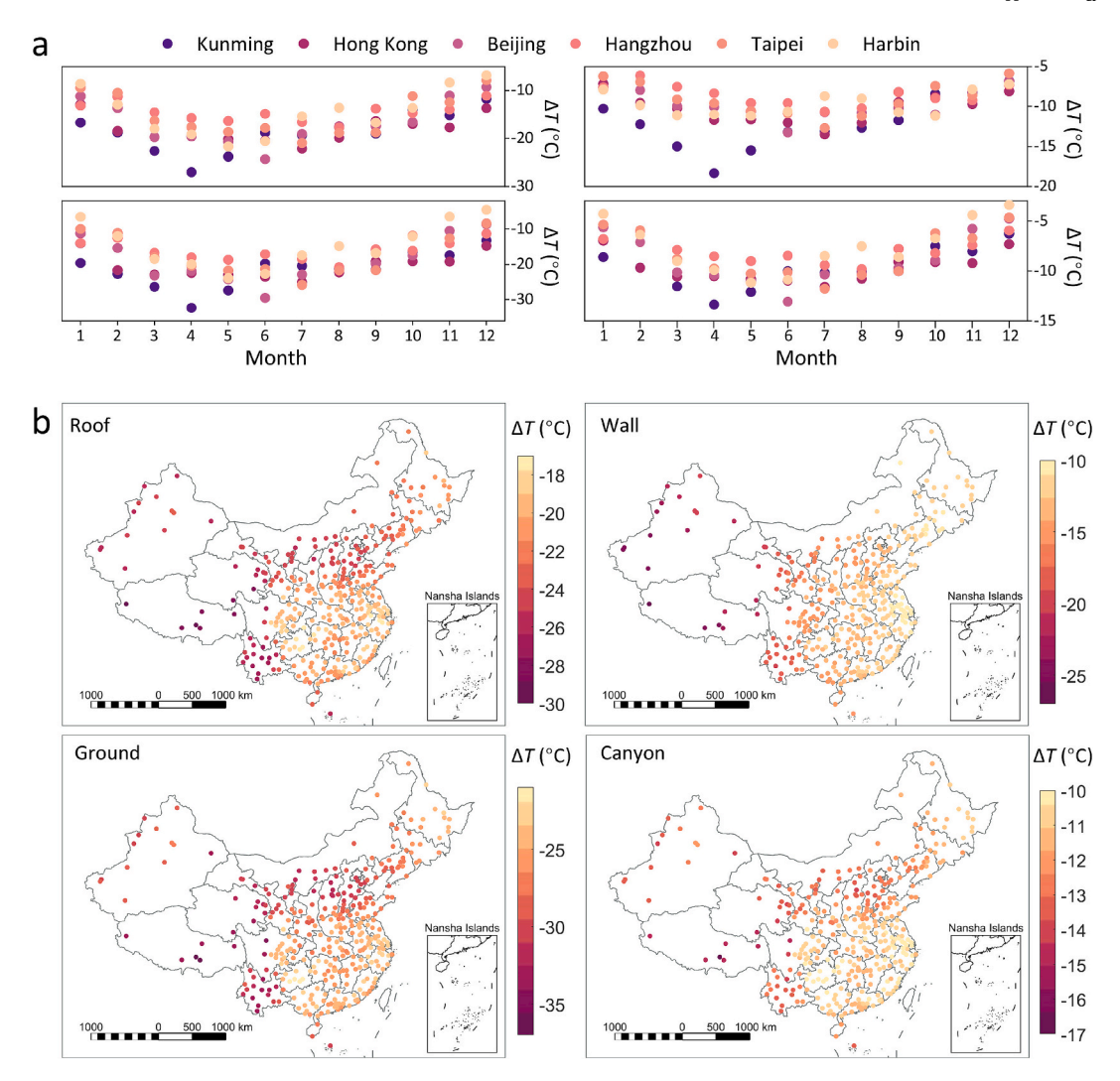


Fig. 6. Maximum surface temperature reductions in China. (a) Monthly cooling effects of RC coatings in six representative cities across distinct climate zones. (b) National map showing temperature reductions for rooftops, walls, ground, and canyon areas.

benefits from numerous clear days with minimal cloud cover, enhancing solar intensity. Additionally, Harbin, a representative city in these cold zones, experiences long, harsh winters and short, cool summers with abundant solar radiation. Under such conditions, RC coatings demonstrate significant cooling effects. Conversely, the south-eastern coastal regions exhibit weaker cooling performance of RC coatings due to lower solar radiation intensity. For instance, Hong Kong experiences its peak average direct solar radiation in July, reaching approximately 288  $W \cdot m^{-2}$ , which limits the cooling potential. In contrast, Kunming achieves the most significant temperature reduction in April, benefitting from an average direct solar radiation of 403 W·m $^{-2}$ , while other cities during the same period receive only 190 to 240 W·m $^{-2}$ . Moreover, these coatings are particularly effective during the warmer months of May to August, when cities experience maximum solar radiation levels. These findings highlight how regional variations in solar exposure and climatic conditions influence the effectiveness of RC coatings, underscoring the importance of tailored strategies for different locales. However, assessing the performance of these coatings should not be based solely on cooling potential; it is imperative to analyze the annual energy savings they offer. Consequently, the following section delves into the energysaving potential of RC coatings, emphasizing their broader impact on urban energy efficiency.

#### 4.4. Buildings cumulative heat flux and Electricity Savings in China

To effectively implement RC coatings across various Chinese cities, it is crucial to assess their annual energy-saving performance, thereby determining their suitability in different regions rather than applying them uniformly nationwide. Using the UCM and focusing on office buildings, the cumulative heat fluxes for rooftops and walls was calculated compared with that of no paint. Based on national heating coverage and policies, whether RC coatings lead to net energy savings or increased energy consumption over time was evaluated. The distribution of centralized heating periods is illustrated in Fig. 7. Specifically, in Harbin, the yearly heating season extends from October 20 to April 20 of the following year; in Zhengzhou, from November 15 to March 15 of the following year; and in Hefei, from December 5 to March 5 of the following year. During these heating seasons in northern cities, reductions in heat gain due to RC coatings are considered to increase energy consumption, as they may increase heating demands. Conversely, in other seasons, these reductions contribute to energy savings by lowering cooling loads. In southern regions like Guangdong, where heating demand is minimal from December to February and no additional cooling is needed, RC coatings are considered to have a negligible effect. To evaluate the energy savings provided by RC coatings in office buildings, the electricity saving was calculated using the coefficient of performance (COP) for heating and the energy efficiency ratio (EER) for cooling, assumed to be 1.8 and 2.9, respectively [47].

Z. Li et al. Applied Energy 393 (2025) 126138

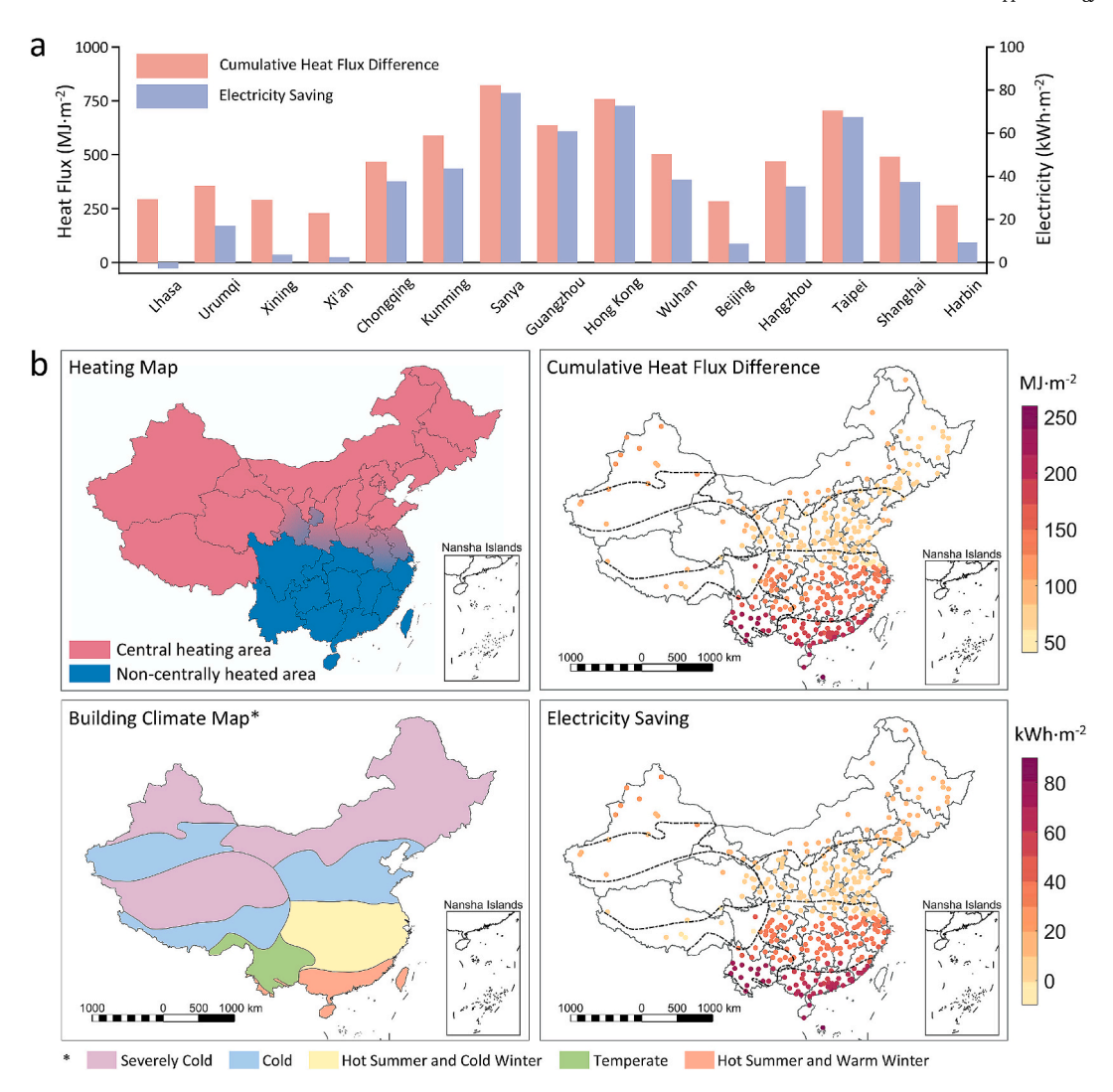


Fig. 7. Cumulative heat flux and electricity savings in China. (a) Cumulative heat flux and electricity savings in fifteen representative cities. (b) Map of China showing cumulative heat flux and electricity savings, along with boundaries of building climate zones. The left two figures depict the centralized heating regions and building climate zones in China.

Detailed results of the analysis are presented in Fig. 7.

Fig. 7a presents the cumulative heat flux and corresponding electricity savings for fifteen representative cities across China. Analysis of data from Fig. 6b reveals that cities such as Lhasa and Ürümgi, characterized by cooler and drier climates, exhibit enhanced cooling effects from RC coatings during the summer months. However, their overall annual benefits are diminished due to significant heating demands in winter, which counteract the summer savings. Notably, in Lhasa, the application of RC coatings can even lead to an increase in annual electricity consumption. Similarly, cities like Xining, Xi'an, and Beijing show minimal electricity savings due to their specific climatic conditions. In contrast, subtropical cities like Hong Kong, with milder winters and consistent year-round cooling demands, derive substantial benefits from RC coatings. The coatings provide steady energy savings throughout the year, enhancing their overall effectiveness in these regions. Fig. 7b displays maps of cumulative heat flux and electricity savings across China. Notably, the contours observed closely align with the country's building climate zones, forming a clear boundary near the Oinling-Huaihe line, which demarcates the geographical division between northern and southern China in terms of climate and heating practices. RC coatings offer significant benefits in temperate regions, as well as in areas with hot summers and cold winters and those with hot summers and warm winters, making them ideal for year-round use due to their consistent cooling effects that enhance energy efficiency. Conversely, their effectiveness is less pronounced in other climate zones, particularly in colder regions like Lhasa, where winter heating demands offset the summer cooling benefits provided by RC coatings. Therefore, the application of RC coatings is closely linked to climate conditions and regional heating practices. Focusing on warmer areas will maximize the benefits of RC coatings by providing substantial year-round energy savings.

#### 5. Conclusion

This study proposed a novel RC-coupled UCM model designed to assess the efficacy of RC coatings in alleviating the UHI effect across diverse urban climates in China. Through a comprehensive evaluation of RC coating performance on various urban surfaces in varied climatic conditions and urban configurations, a strategic application approach was advocated that enhances energy efficiency, providing year-round energy savings. This approach entails precision-targeting the application of suitable RC coatings on designated streets within distinct building climate zones in China, effectively mitigating UHI impacts across a range of climatic contexts.

These findings underscore the pivotal role of solar reflectance in amplifying cooling efficacy, as higher reflectance effectively deflects a Z. Li et al. Applied Energy 393 (2025) 126138

 $q_{\rm sun}$ 

significant portion of incoming solar radiation. In contrast, the influence of emissivity within the atmospheric window on overall cooling capacity is comparatively minor. Thus, the optimization of RC coatings' spectral properties in the solar spectrum emerges as a critical factor in maximizing their effectiveness in urban environments. Moreover, urban geometry exerts a substantial impact on the performance of RC coatings due to its effects on solar exposure and shading. Lower aspect ratios facilitate increased solar exposure, thereby augmenting cooling effects on rooftops and ground surfaces. Conversely, higher aspect ratios heighten shading, diminishing the efficacy of the coatings. To optimize cooling efficiency, the application of RC coatings on the ground in wider streets and on the walls of both sides in narrower streets was recommend. This strategic deployment capitalizes on the optimal solar radiation exposure for each surface, thereby enhancing the overall performance of RC coatings.

The effectiveness of RC coatings is further influenced by climatic conditions. Cities in north-western China, characterized by intense solar radiation, experience the most significant cooling benefit from these coatings. Conversely, south-eastern coastal cities, despite their higher average air temperatures, exhibit weaker cooling effects due to lower solar radiation. Seasonal fluctuations also significantly impact annual energy consumption. In subtropical regions such as Hong Kong, where cooling demands persist throughout the year, RC coatings provide consistent and stable energy savings. However, in colder regions, while RC coatings can deliver substantial cooling benefits during the summer months, they may inadvertently increase heating requirements in winter, potentially offsetting the energy savings achieved during the summer period.

In conclusion, the efficacy of RC coatings hinges on a combination of material optical properties, urban configurations, and regional climate dynamics. Optimal cooling efficiency of RC coatings can be achieved by prioritizing materials with high solar spectrum reflectance and tactically applying them considering factors such as street dimensions, building heights, and orientations. Concentrating efforts on areas characterized by hot-summers/warm-winters and hot-summers/cold-winters promises to maximize the advantages of RC coatings, yielding substantial yearround energy savings. Future research endeavors should concentrate on the development of adaptive RC materials capable of adjusting to seasonal temperature fluctuations, ensuring sustained energy efficiency enhancements across diverse environmental contexts.

#### Nomenclature

L NMBE

AH	Anthropogenic heat flux (W·m <sup>-2</sup> )
$c_{\mathrm{R}}$	Heat capacity of roof (MJ·K $^{-1}$ ·m $^{-3}$ )
c <sub>W</sub>	Heat capacity of wall (MJ·K <sup>-1</sup> ·m <sup>-3</sup> )
$c_{ m G}$	Heat capacity of ground ( $MJ \cdot K^{-1} \cdot m^{-3}$ )
-	E] Coefficient of variation of the root-mean-square error
COP	Coefficients of performance
d	Day number of the year
$d_{ m R}$	Thickness of roof (m)
$d_{\mathrm{W}}$	Thickness of wall (m)
$d_T$	Displacement height (m)
EER	Energy efficiency ratio
h	Normalized building height
H	Building height
HR	High-reflectance
$k_{ m R}$	Thermal conductivity of roof $(W \cdot K^{-1} \cdot m^{-1})$
$k_{ m W}$	Thermal conductivity of wall (W·K <sup>-1</sup> ·m <sup>-1</sup> )
$k_{ m G}$	Thermal conductivity of ground $(W \cdot K^{-1} \cdot m^{-1})$
$l_{\rm s}$	Normalized shadow

PP Phosphorescent Downwelling longwave radiation (W⋅m<sup>-2</sup>)  $q_{\rm atm}$ 

Longwave radiation (W⋅m<sup>-2</sup>)

Normalized mean bias error

Radiative thermal load of the emitter  $(W \cdot m^{-2})$ 

Conductive heat flux (W·m<sup>-2</sup>)  $Q_{\rm G}$ Sensible heat flux (W·m<sup>-2</sup>)  $Q_{H}$ Latent heat flux (W·m<sup>-2</sup>)  $Q_{\rm LE}$ Urban canyon aerodynamic resistance (s⋅m<sup>-1</sup>)  $R_{\rm C}$ Net radiation  $(W \cdot m^{-2})$  $R_n$ Radiative cooling RC RR Retro-reflective Solar radiation (W $\cdot$ m $^{-2}$ ) S Direct solar radiation (W⋅m<sup>-2</sup>)  $S_{\rm B}$ Diffuse solar radiation (W⋅m<sup>-2</sup>)  $S_{\mathrm{D}}$ Time (hour) t T Temperature (K) Friction velocity (m·s<sup>-1</sup>) 11× Roof-level wind speed (m·s<sup>-1</sup>)  $u_{R}$ Canyon-level wind speed (m·s<sup>-1</sup>)  $u_{\rm C}$ UCM Urban canopy model UHI Urban heat island w Normalized canyon width zHeight (m) Reference level (m)  $z_{\mathrm{Ref}}$ Canyon momentum roughness length (m)  $z_{\rm m,C}$ Roof momentum roughness length (m)  $z_{\rm m,R}$ Canyon heat roughness length (m)  $z_{h,C}$ Roof heat roughness length (m)  $z_{h,R}$ Effective roughness length (m)  $z_{OT}$ 

Absorbed incident solar radiation (W·m<sup>-2</sup>)

#### Greek symbols

Intitudo (mod)

$\varphi$	Lautude (rad)
$\varphi_r$	Latitude of the tropic of cancer (rad)
$\theta_{ m az}$	Solar azimuth angle (rad)
$\theta_{\mathrm{z}}$	Solar zenith angle (rad)
$ heta_{ m C}$	Canyon orientation (rad)
$\theta$	Difference between the solar azimuth and canyon orientation
	(rad)
κ	von Karman constant
δ	Solar declination (rad)
$\delta_{ m R}$	Thickness of the internal boundary layer (m)
$\omega_{t}$	Solar hour angle (rad)

#### Subscripts

C	Urban canyon
G	Ground
R	Building roof
S	Sky
W	Wall

#### CRediT authorship contribution statement

Ze Li: Writing - original draft, Visualization, Methodology, Formal analysis, Data curation. Jianheng Chen: Writing - review & editing. Chuyao Wang: Writing - review & editing. Wenqi Wang: Writing review & editing. Yang Fu: Writing - review & editing. Xu Chen: Validation. Rui Zhang: Validation. Aiqiang Pan: Validation. Tsz Chung Ho: Validation. Kaixin Lin: Validation. Lin Liang: Validation. Chi Yan Tso: Writing - review & editing, Funding acquisition.

#### **Declaration of competing interest**

The authors declare that they have no known competing financial interests or personal relationships that could have appeared to influence the work reported in this paper.

#### Acknowledgments

This work was supported by the Hong Kong Research Grant Council via Research Fellow Scheme with the reference number of RFS2425-1S06, and via the Strategic Topics Grant (STG) account STG2/E-605/23-N, as well as by the Innovation and Technology Commission via Innovation and Technology Fund (ITF) account ITS/128/22FP.

#### Data availability

The weather data used in this study is open data from ECWMF EAR5 https://cds.climate.copernicus.eu/datasets. All data can be downloaded through python or directly from the website.

#### References

- [1] Wahba Tadros SN, et al. Demographic trends and urbanization (English). 2021.
- [2] Arnfield AJ. Two decades of urban climate research: a review of turbulence, exchanges of energy and water, and the urban heat island. Int J Climatol 2003;23 (1):1–26
- [3] Kleerekoper L, Van Esch M, Salcedo TB. How to make a city climate-proof, addressing the urban heat island effect. Resour Conserv Recycl 2012;64:30–8.
- [4] Croce S, Vettorato D. Urban surface uses for climate resilient and sustainable cities: a catalogue of solutions. Sustain Cities Soc 2021;75:103313.
- [5] Kim SW, Brown RD. Urban heat island (UHI) intensity and magnitude estimations: a systematic literature review. Sci Total Environ 2021;779:146389.
- [6] Wang Z-H. Reconceptualizing urban heat island: beyond the urban-rural dichotomy. Sustain Cities Soc 2022;77:103581.
- [7] Yang Y, et al. Quantitative analysis and prediction of urban heat island intensity on urban-rural gradient: a case study of Shanghai. Sci Total Environ 2022;829: 154964
- [8] Li X, et al. Urban heat island impacts on building energy consumption: a review of approaches and findings. Energy 2019;174:407–19.
- [9] Verichev K, Salazar-Concha C, Díaz-López C, Carpio M. The influence of the urban heat island effect on the energy performance of residential buildings in a city with an oceanic climate during the summer period: case of Valdivia. Chile Sustainable Cities and Society 2023;97:104766.
- [10] Lemonsu A, Viguie V, Daniel M, Masson V. Vulnerability to heat waves: impact of urban expansion scenarios on urban heat island and heat stress in Paris (France). Urban Clim 2015;14:586–605.
- [11] Harmay NSM, Choi M. The urban heat island and thermal heat stress correlate with climate dynamics and energy budget variations in multiple urban environments. Sustain Cities Soc 2023;91:104422.
- [12] Ward K, Lauf S, Kleinschmit B, Endlicher W. Heat waves and urban heat islands in Europe: a review of relevant drivers. Sci Total Environ 2016;569:527–39.
- [13] Ho JY, et al. Urban heat island effect-related mortality under extreme heat and non-extreme heat scenarios: a 2010–2019 case study in Hong Kong. Sci Total Environ 2023;858:159791.
- [14] Wong LP, et al. Urban heat island experience, control measures and health impact: a survey among working community in the city of Kuala Lumpur. Sustain Cities Soc 2017;35:660–8.
- [15] Vicedo-Cabrera AM, et al. The burden of heat-related mortality attributable to recent human-induced climate change. Nat Clim Chang 2021;11(6):492–500.
- [16] Gunawardena KR, Wells MJ, Kershaw T. Utilising green and bluespace to mitigate urban heat island intensity. Sci Total Environ 2017;584:1040–55.
- [17] Wu CY, et al. Understanding the relationship between urban blue infrastructure and land surface temperature. Sci Total Environ 2019;694.
- [18] Wang C, Wang Z-H, Kaloush KE, Shacat J. Cool pavements for urban heat island mitigation: a synthetic review. Renew Sust Energ Rev 2021;146:111171.
- [19] Sen S, Khazanovich L. Limited application of reflective surfaces can mitigate urban heat pollution. Nat Commun 2021;12(1).

- [20] Schneider FA, et al. Evidence-based guidance on reflective pavement for urban heat mitigation in Arizona. Nat Commun 2023;14(1).
- [21] Rossi F, et al. Analysis of retro-reflective surfaces for urban heat island mitigation: a new analytical model. Appl Energy 2014;114:621–31.
- [22] Huang X, et al. Optimizing retro-reflective surfaces to untrap radiation and cool cities. Nature Cities 2024;1(4):275–85.
- [23] Chiatti C, et al. Exploring the potential of phosphorescence for mitigating urban overheating: first time representation in an urban canopy model. Appl Energy 2024;362.
- [24] Fabiani C, et al. Adaptive measures for mitigating urban heat islands: the potential of thermochromic materials to control roofing energy balance. Appl Energy 2019; 247:155–70.
- [25] Raman AP, et al. Passive radiative cooling below ambient air temperature under direct sunlight. Nature 2014;515(7528):540–4.
- [26] Zhai Y, et al. Scalable-manufactured randomized glass-polymer hybrid metamaterial for daytime radiative cooling. Science 2017;355(6329).
- [27] Mandal J, et al. Hierarchically porous polymer coatings for highly efficient passive daytime radiative cooling. Science 2018;362(6412):315–8.
- [28] Zhao DL, et al. Subambient cooling of water: toward real-world applications of daytime radiative cooling. Joule 2019;3(1):111–23.
- [29] Lin KX, et al. Hierarchically structured passive radiative cooling ceramic with high solar reflectivity. Science 2023;382(6671):691–7.
- [30] Wang WQ, et al. Enhancing cold energy harvest with daytime passive radiative cooling and phase change materials integration: a numerical exploration. Appl Therm Eng 2024;249.
- [31] Vilà R, Medrano M, Castell A. Mapping nighttime and all-day radiative cooling potential in europe and the influence of solar reflectivity. Atmosphere 2021;12(9):
- [32] Li M, Peterson HB, Coimbra CF. Radiative cooling resource maps for the contiguous United States. Journal of Renewable and Sustainable Energy 2019;11(3).
- [33] Liu J, et al. Field investigation and performance evaluation of sub-ambient radiative cooling in low latitude seaside. Renew Energy 2020;155:90–9.
- [34] Chen JH, Lu L, Gong Q. A new study on passive radiative sky cooling resource maps of China. Energy Convers Manag 2021;237.
- [35] Pirvaram A, Talebzadeh N, Leung SN, O'Brien PG. Radiative cooling for buildings: a review of techno-enviro-economics and life-cycle assessment methods. Renew Sust Energ Rev 2022:162:112415.
- [36] Chen J, et al. Techno-economic and environmental performance assessment of radiative sky cooling-based super-cool roof applications in China. Energy Convers Manag 2021;245:114621.
- [37] Jiang T, et al. Experimental study and thermo-economic analysis of a novel radiant-convective cooling system. Int J Refrig 2021;131:505–14.
- [38] Li H, Zhang J, Liu X, Zhang T. Comparative investigation of energy-saving potential and technical economy of rooftop radiative cooling and photovoltaic systems. Appl Energy 2022;328:120181.
- [39] Zhou K, Miljkovic N, Cai L. Performance analysis on system-level integration and operation of daytime radiative cooling technology for air-conditioning in buildings. Energ Buildings 2021;235:110749.
- [40] Wang ZH, Bou-Zeid E, Smith JA. A coupled energy transport and hydrological model for urban canopies evaluated using a wireless sensor network. Q J R Meteorol Soc 2013;139(675):1643–57.
- [41] Harman IN, Barlow JF, Belcher SE. Scalar fluxes from urban street canyons. Part II: Model Boundary-Layer Meteorology 2004;113(3):387–409.
- [42] Von Karman T. Progress in the statistical theory of turbulence. Proc Natl Acad Sci 1948;34(11):530–9.
- [43] Masson V. A physically-based scheme for the urban energy budget in atmospheric models. Bound-Layer Meteorol 2000;94(3):357–97.
- [44] Fan SH, Li W. Photonics and thermodynamics concepts in radiative cooling. Nat Photonics 2022;16(3):182–90.
- [45] Hersbach H, et al. ERA5 hourly data on single levels from 1940 to present. Copernicus Climate Change Service (C3S) Climate Data Store (CDS). 2023.
- [46] Jing J, et al. The spatial distribution of China's solar energy resources and the optimum tilt angle and power generation potential of PV systems. Energy Convers Manag 2023;283:116912.
- [47] Wang CY, Yang HX, Ji J. Performance analysis of a PV/T shading device for enhancing energy saving and human comfort. Appl Energy 2024;376.